

Embedded Microjets for Thermal Management of High Power-Density Electronic Devices

Stephen M. Walsh, *Student Member, IEEE*, Bernard A. Malouin Jr., Eric A. Browne, Kevin R. Bagnall, Evelyn N. Wang, and James P. Smith

Abstract—With current trends toward increased power in smaller devices and packages, the search continues for high performance thermal management solutions for MOSFETs, HEMTs, and other power electronics. Microjet impingement cooling has been shown to produce high heat transfer capabilities for electronics cooling. In this work, microjets based on well-studied geometries were embedded within the substrate of a heat-producing device, removing several layers of thermal resistance typically found in advanced packages. In contrast with competing liquid cooling solutions that use expensive materials and processes, industry-standard silicon microfabrication techniques were used to build a low cost microjet cooler. Numerical analysis of the embedded microjet device showed average heat transfer coefficients greater than $250 \text{ kW/m}^2\text{-K}$ and low peak temperature rises in high power-density devices. Using an innovative micro-Raman thermography technique, experimental measurements with $1 \mu\text{m}$ spatial resolution were taken, supporting the numerically predicted heat transfer coefficients on a device with a heat flux of over 5 kW/cm^2 and a temperature rise of $46 \text{ }^\circ\text{C}$. As devices continue to become miniaturized, both low cost embedded microjet cooling technology and micro-Raman thermography may play a vital role in the design, operation, and evaluation of advanced high power-density electronics.

Index Terms—Electronics cooling, thermal management of electronics, electronics packaging, microjet impingement, single-phase cooling, Raman thermography, silicon devices, HEMTs, microfluidics.

I. INTRODUCTION

IMPROVEMENT in the materials, processes, and designs of semiconductors has led to the shrinking of device characteristic dimensions from micrometers to nanometers, leading to a high density of transistors. At the die level, power dissipation can result in localized hot spots with length scales of only a few micrometers, in which the power density can reach 5 to $10\times$ the average die power density [1]. Meanwhile, the peak temperatures experienced in these localized hot spots dictate reliability of the device. Thermal considerations thus become a limiting factor in both the initial implementation and continued operation of devices. One such device is a gallium nitride (GaN) high electron mobility transistor (HEMT) used in high power radio frequency (RF) components, capable of a linear power density of 40 W/mm [2].

Manuscript received January 30, 2018; revised June 26, 2018; accepted August 27, 2018. This work was sponsored by the Department of the Air Force under Air Force Contract No. FA8721-05-C-0002. Opinions, interpretations, conclusions, and recommendations are those of the authors and are not necessarily endorsed by the United States Government.

S. M. Walsh, B. A. Malouin, E. A. Browne, K. R. Bagnall and J. P. Smith are with Lincoln Laboratory, Massachusetts Institute of Technology, Lexington, MA 02421 USA (email: stephen.walsh@ll.mit.edu; bernie.malouin@ll.mit.edu; eric.browne@ll.mit.edu; kevin.bagnall@ll.mit.edu; jim.smith@ll.mit.edu).

S. M. Walsh and E. N. Wang are with the Department of Mechanical Engineering, Massachusetts Institute of Technology, Cambridge, MA 02139 USA (email: enwang@mit.edu).

Recent state-of-the-art cooling of such devices has been achieved through the use of liquid cooling at the substrate level with advanced materials and processes. A team led by Northrop-Grumman incorporated diamond lined microchannels and jets etched into silicon to dissipate 1.16 kW/cm^2 at the die level [3]. A team led by Raytheon cooled a GaN-on-diamond device fabricated on diamond microchannels with a heat flux of 1.23 kW/cm^2 [4]. A team led by Lockheed-Martin fabricated a palladium jet impingement manifold with additive manufacturing, dissipating a heat flux of 1.0 kW/cm^2 [5–6]. In contrast with the preceding work, this manuscript reports on embedded cooling where the jet array is fabricated using low-cost, high-volume, industry-standard silicon fabrication techniques.

The exceptional heat transfer performance of jet impingement, shown in Fig. 1, has been the subject of extensive research for several decades [7–10]. Sung and Mudawar identified advantages of jet impingement over microchannels as higher heat transfer coefficients, lower pressure drops, and the ability to achieve uniform temperature distributions when used in arrays [11].

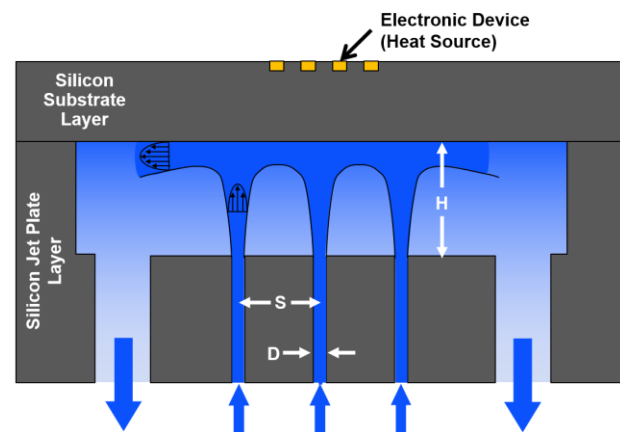


Fig. 1. Embedded microjet impingement is integrated within the device substrate, cooling the backside of the heat generating element at the top of the stackup. The fluid impinges through narrow passages into a fluid-filled cavity and exits through the larger exit ports shown. This approach produces a high performance, low size, weight, and power (SWaP) thermal solution for high power-density electronics.

Microjets are a form of jet impingement, where a column of fluid at a higher velocity than its surroundings, and initially less than a millimeter in diameter, interacts with a solid surface. The presence of the surface causes the fluid velocity to be stagnated where the jet centerline intersects the wall. Within this stagnation zone, the thermal boundary layer is compressed as the pressure increases and the flow is accelerated parallel to the surface. With the boundary layer compression (and flow redirection) in the stagnation zone comes high heat transfer coefficients. This study used submerged microjets, where the jet issues into an enclosed cavity filled with the same fluid of which the jet is comprised. Submerged jets are immediately influenced by the viscosity of the surrounding fluid. The jet velocity profile becomes a larger diameter, and viscous effects lead to entrainment of surrounding fluid. This jet spreading is manifested through a larger stagnation area, with high thermal performance [12].

Microjets can be used individually or organized in two-dimensional arrays. Arrays allow for more area to be subjected to high heat transfer coefficients, producing greater overall heat transfer and greater uniformity in temperature. Several geometrical parameters shown in Fig. 1 influence the jet impingement performance including jet diameter (D), jet-to-jet spacing (S), and jet-to-target distance (H). Numerous researchers have performed experimental investigations and optimizations of jet array geometry. Browne et al. investigated arrays of 54 and 112 μm diameter microjets arranged in a 4×4 array at various flow rates [13]. Fabbri and Dhir explored microjet arrays with diameters ranging from 69 to 250 μm [14]. Brunswiler et al. studied a branched array with diameters ranging from 31 to 126 μm [15].

While studying the parametric landscape, Robinson and Schnitzler performed an experimental characterization of an array of 1 mm jets, varying jet-to-jet and jet-to-target distances

[16]. In submerged jets, the heat transfer performance was insensitive to changes in jet-to-target (i.e., standoff) distances from approximately 2 to 3 jet diameters. At a fixed jet-to-target distance of 2 jet diameters, the jet-to-jet spacing, or pitch, was changed from 7 jet diameters to 3 jet diameters and performance increased by approximately 10%. This result was consistent with the results of previous researchers [17–19], which showed that microjets arranged with jet-to-jet spacing and jet-to-target distances of ~ 2 jet diameters achieved the highest performance of arrays studied.

In this work, the insight gathered from the aforementioned researchers was leveraged to produce a high performance microjet array design. This microjet array was then realized within the substrate of a silicon test device, using low-cost silicon fabrication techniques.

II. THE MICROJET DEVICE

A. Design of the Microjet Array and Integrated Heater

A test device, shown in Fig. 2, was built to characterize the performance of the embedded microjet cooling. The device consisted of a microjet array and an integrated heater. The microjet array was designed based on previous jet impingement heat transfer studies. The integrated heater was designed to match the geometrical and power density aspects of advanced electronic devices, such as multifingered GaN HEMTs used in power amplifiers for RF applications.

As discussed in Section I, the geometry of arrays of microjets has been the subject of extensive optimizations and experimental investigations. Building on conclusions of previous researchers, an initial geometry was chosen such that the jet diameter was 116 μm , the jet-to-jet distance was 190 μm (1.64 jet diameters) and the jet-to-target distance was 200 μm (1.72 jet diameters). The jet-to-jet spacing was chosen because

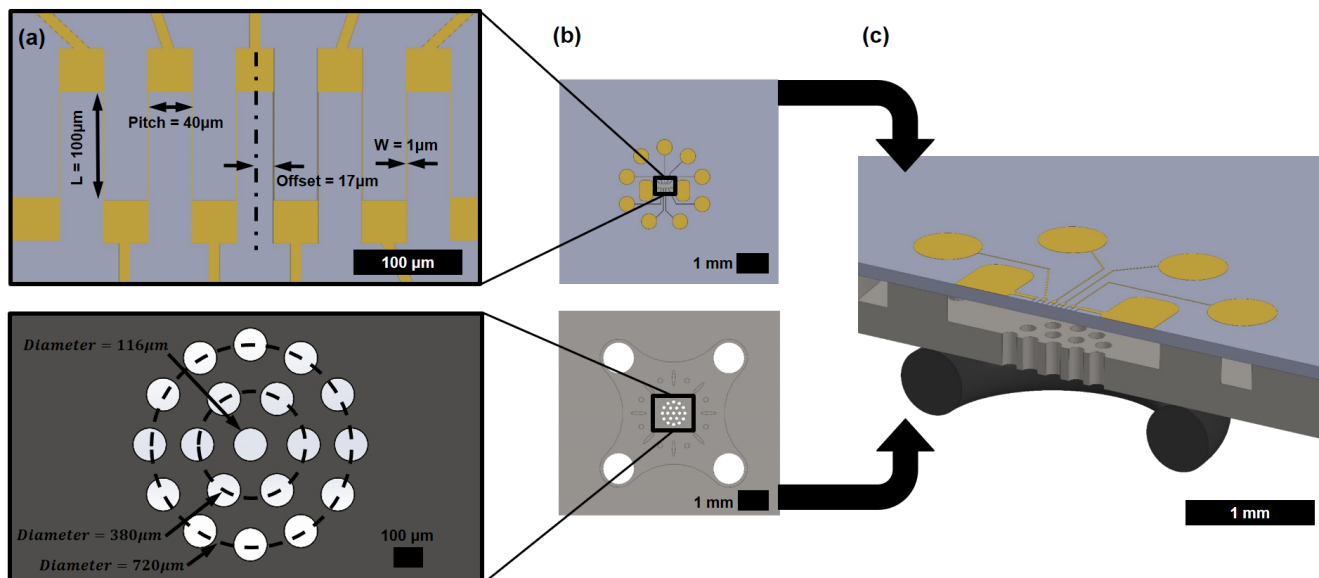


Fig. 2. (a) Top image shows the geometry of the high power-density heater die, which is a resistive heater. The heater is designed such that the geometry of the ten high resistance finger-like segments that dissipate heat replicates the geometry of advanced electronic devices. While overall power applied is modest (~ 2 W), the power density becomes high (>5 kW/cm²) owing to the small feature sizes. Bottom image shows the array of 19 microjets of 116 μm diameter arranged in two concentric rings of 720 μm and 380 μm diameters, with one microjet at the center. (b) Top image shows an increased scale depiction of the heater die showing the ring of contact pads used to apply power to the device. Bottom image shows an increased scale depiction of the microjet die, which shows the 200 μm deep well. The ring of support features guide the flow and provide structural strength. At the four outer corners are larger (1 mm diameter) exhaust ports. (c) The full assembly of the microjet cooled device consists of the heater die and microjet array die, bonded together. Coolant fluid, contained by an O-ring, flows up through the array of orifices to impinge upon the backside of the heater die, providing very high heat transfer coefficients.

the heat transfer performance has been shown to improve with decreasing spacing for a given fluid flow rate, but the spacing was not too close where the microjets would interact before impingement. The jet-to-target spacing was chosen to balance the microjets being sufficiently spread to cover an appreciable impingement zone while not being overly spread to the point where impingement velocities are greatly reduced, and heat transfer suffers [16]. The array consisted of 19 microjets, arranged with 12 microjets on an outer circle (720 μm diameter), 7 microjets on an inner circle (380 μm diameter), and one microjet in the center, shown in the planform view of the microjets in Fig. 2a.

The clover-leaf well geometry was qualitatively designed to passively guide the fluid streamlines from the microjet array to the large exhaust ports (1 mm diameter) located in each of the four corners. The exhaust ports were sized such that the cumulative cross sectional area of the exhaust ports was an order of magnitude larger than the cumulative microjet cross sectional area. This design minimizes the required driving pressure, and the pressure losses within the device were localized to the microjets. Surrounding the array of circular microjets (but inside the exhaust port pattern) exists an array of pillars. These pillars serve several functions: they provide support structure within the well, and they nominally increase surface area while guiding the flow to the exhaust ports. The structural support function becomes more important for the completed assembly, where devices were installed into a test apparatus with micro O-rings.

The resistive heater was designed to emulate an integrated circuit found in advanced, high power-density electronics. The design of the heater was based on the power dissipation profile of multifinger GaN HEMTs which are commonly used in power amplifiers for RF communication or other RF applications [20–21]. This power dissipation profile is characterized by a high amount of heat generation localized around each gate finger. The geometry used for the integrated heater in this study is shown in Fig. 2a. The heater formed a circuit comprised of 10 finger-like segments of high resistance, connected in series by lower resistance pads. The high resistance segments of Titanium Nitride (TiN) were 1 μm wide and 100 μm long. The high resistance segments were connected by lower resistance pads, each with less than 1% of the resistance of the finger-like segments, concentrating the Joule heating to the very narrow finger-like sections. This concentration created a row of ten high power-density linear segments, with modest overall power dissipation (1.95 W), but with very high power density ($>5 \text{ kW}/\text{cm}^2$).

B. Fabrication and Bonding

The microjets were fabricated in a 450 μm thick silicon substrate. In this substrate, a 200 μm deep clover-leaf shaped well was etched into one side of the silicon, as illustrated in Fig. 2c. In the final assembly, this well formed the fluid plenum between the microjet die and the high power-density heater die. At the center of this well, the circular array of microjet orifices was etched through the remaining 250 μm of silicon. The microjets were diced into 20 mm \times 20 mm dies.

The high power-density heater was fabricated with a 150 nm thick titanium nitride (TiN) ceramic heater deposited on the top surface of a silicon substrate. The substrate was thinned to a

total thickness of 200 μm and encapsulated with a plasma-enhanced chemical vapor deposition (PECVD) SiO_2 protective oxide, which covered the top of the heater traces for protection. Ohmic contact pads, opened through the oxide, were located around the heater circuit, plated with 500 nm of gold, and were used to deliver a driving potential to the heater by way of DC probe tips on micro-manipulators. Similar to the microjet dies, the high power-density heaters were diced into 20 mm \times 20 mm dies.

To assemble the microjet-cooled test device, the high power-density dies and the microjet dies were aligned and bonded together. Alignment between the two dies can be accomplished with metallic fiducials, proper fixturing, or by visual alignment. By design, the alignment of the microjet array to the device does not require precise alignment, as the circular array produces an impingement zone of almost 1 mm \times 1 mm on the back side of the device (i.e., much larger than the heated zone). While the highest heat transfer coefficients are located at the stagnation point of the jet centerline, heat transfer coefficients remain high moving radially outward, minimizing radial temperature gradients in the device (i.e., a gradual radial degradation in thermal performance). In these experiments, devices were aligned to within 100 μm by use of custom fixturing.

Given the smooth surfaces of each die, several strategies are available to bond the dies. Direct fusion bonding, eutectic gold bonds, indium solders, or industrial adhesives may be used. As the bond line does not participate in the thermal path (i.e., microjets impinge directly on the backside of the heaters, not through the bond), the bond material is not important for thermal performance. This key attribute allows device designers and process engineers to use bonding technologies that are driven by the device process flow, and not by thermal requirements. Here, the two dies have been bonded with industrial adhesive (Loctite 406).

III. NUMERICAL METHODS

A numerical model was developed to predict the performance of the test device, to compare surface temperatures with experimental measurements, and to calculate the convective heat transfer coefficient on the impingement surface. COMSOL Multiphysics 5.3 was used to solve a fully conjugate computational fluid dynamics (CFD), conduction heat transfer, and convection heat transfer simulation for steady-state non-isothermal flow.

The fluid dynamics were modeled with the Reynolds-averaged Navier-Stokes (RANS) equations for conservation of momentum as a $k-\Omega$, two-equation turbulence model with automatic wall treatment [22]. The COMSOL default turbulence model parameters were used. The $k-\Omega$ model was chosen for its improved accuracy and convergence performance in internal flows with strong curvature, as found in microjets [23]. Conservation of mass was modeled with the continuity equation. Gravity-driven flow due to fluid temperature differences was neglected as the buoyancy forces are small compared with the advective forces. Heat transfer was modeled with the heat equation, including convection in the fluid domain. Two-way multiphysics coupling was defined between the fluid dynamics and heat transfer models with COMSOL's

non-isothermal flow feature and the Kays-Crawford heat transport turbulence model [24].

The simulation domain was divided into a fluid subdomain and a solid subdomain, the latter representing the heater. Quarter symmetry was used for computational efficiency. The full domain is shown in Fig. 3.

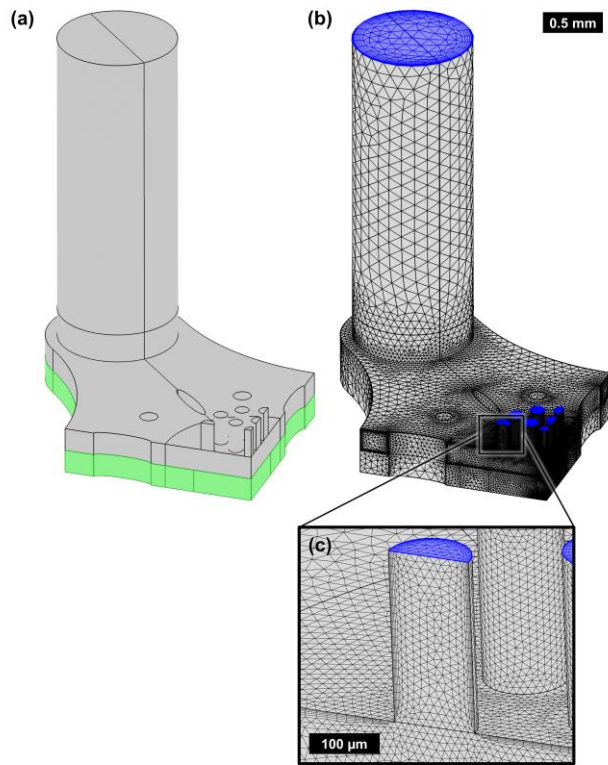


Fig. 3. (a) The quarter-symmetry computational domain is shown, with the solid subdomain (representing the heater die) in green and the fluid domain (including jet orifices and the large exhaust port) in gray. (b, c) The resulting mesh is shown, with inlet and outlet faces highlighted in blue.

The fluid subdomain consists of three regions. First, the majority of the subdomain was defined by the 200 μm deep well enclosed by the microjet die and the heater die. Second, at the origin of the domain, cylinders of diameter $D = 116 \mu\text{m}$ representing the orifices through the microjet die extended 250 μm above the fluid well (i.e., the thickness of the microjet die itself); the top of the cylinder formed the fluid inlet boundary. Finally, downstream, a 1 mm diameter cylinder extended 3 mm above the fluid well, representing the fluid outlet port; the top of this cylinder formed the fluid outlet boundary. The height of this cylinder was chosen so that flow at the outlet was normal to the boundary and unidirectional. Temperature-dependent values for the density (ρ_{fluid}), viscosity (μ), thermal conductivity, and specific heat of liquid water from the COMSOL materials library were used.

The solid subdomain extended 200 μm below the fluid well (i.e., the thickness of the heater die); the remainder of the heater die was not modeled as it lacked a heat source or convective surface and was thus isothermal. Additionally, the ring of support features shown in Fig. 2 was not included in the solid subdomain; heat transfer through these interfaces with the fluid is small compared with heat transfer through the microjet impingement surface. The bottom face of the solid subdomain

was divided into rectangular subregions matching the size and location of the heater's high resistance segments. A thermal conductivity of 150 W/m-K, specific heat of 700 J/kg-K, and density of 2329 kg/m³ (representing silicon) were used.

The computational domain was meshed with free tetrahedral elements and a custom sizing scheme that varied mesh fidelity to accurately capture the large temperature and velocity gradients expected near the high-resistance heater segments and microjet orifices, respectively, while remaining computationally tractable. Mesh sizing was chosen based on the results of a convergence study. For the fluid subdomain, a mesh size range of 6–25 μm was used within and near the microjets (with a maximum element growth rate of 1.05); downstream, a size range of 25–129 μm was used (with a maximum element growth rate of 1.1). The solid subdomain used elements between 12–25 μm with a maximum growth rate of 1.1. Each subdomain used corner refinement with an element size scaling factor of 0.35. Additionally, the fluid subdomain used boundary layer elements to more accurately capture the steep velocity and temperature gradients adjacent to the solid subdomain. The final mesh consisted of 1.3×10^6 elements.

Fluid subdomain boundary conditions were set as a uniform, normal inflow velocity of $V = 16 \text{ m/s}$, representative of flow from a large inlet reservoir. The resulting Reynolds number, Re_D , was:

$$Re_D = \frac{\rho_{\text{fluid}} V D}{\mu} \cong 1900 \quad (1)$$

and the flow was turbulent. Inflow fluid temperature was set at 20 °C. A zero-pressure boundary was enforced on the outlet face. Symmetry boundary conditions were defined as appropriate; no-penetration, no-slip boundaries were defined on all other faces. A steady heat rate of $q = 0.488 \text{ W}$ was applied to the heater's high resistance segments (1.95 W total, accounting for the quarter-symmetry model). An insulation boundary condition (i.e., $q = 0$) was enforced on external surfaces.

Of particular note, because the microjets achieve high performance while remaining single phase, numerical analysis of the system was considerably more tractable and computationally efficient than multiphase approaches. The model was solved on a workstation-class desktop with COMSOL's default convergence criteria in 1.5 hours. After the solution was complete, the results were post-processed to calculate peak temperatures in the heater domain, temperature slices (for comparison to experimental data), and local convective heat transfer coefficients on the 1 mm \times 1 mm impingement zone above the microjet orifices.

IV. EXPERIMENTAL METHODS

A. Thermo-Fluidic System

To examine the performance of the microjet test device, a closed flow loop (Fig. 4a) was constructed to deliver water to the embedded microjets described in Section II. The setup was instrumented to take flow characterization measurements, including the fluid pressure, temperature, and flow rate.

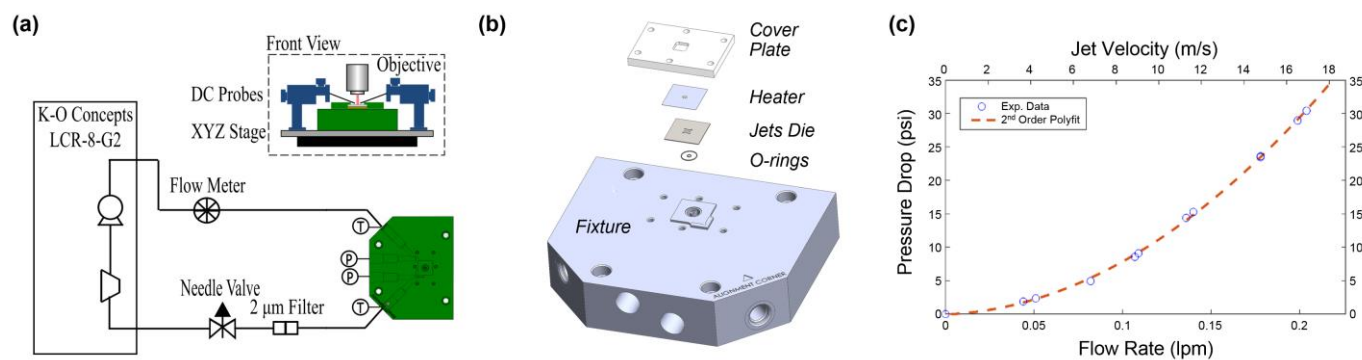


Fig. 4. (a) Schematic of the closed flow loop and front view of the fixture positioned under the Raman microscope with DC probes on custom manipulators to apply power to the device. The flow loop includes a chiller to circulate the fluid and equipment to control and measure the flow rate. (b) Exploded view showing the fixturing used to hold the heater in place as jets impinge vertically upward. (c) Driving pressure required for achieving flow rates, shown both in bulk flow rate in lpm on the bottom axis and velocity at the jet orifice in m/s on the top axis.

A custom test fixture, oversized to accommodate instrumentation, made of polyether ether ketone (PEEK) was designed and fabricated to hold the test device. This fixture provided fluid manifolding to the microjets and featured ports for fluidic measurements. PEEK is a dimensionally stable, high melting point (343 °C) plastic with a low thermal conductivity (0.25 W/m-K) to minimize conduction losses in the system. A fluid inlet channel was bored into the side of the fixture, where it met with an inner cylinder bored from the top side. This inner cylinder engulfed the entire microjet array, which was centered on the fixture. An outer annulus captured the exit port effluent of the microjet array, routing it to the fluid outlet channel on the opposite side of the fixture. O-rings on the inner and outer cylinders created fluidic seals to isolate the incoming fluid from the outgoing effluent. A cover plate was fabricated to provide a compressive sealing force. The microjets ejected vertically upward toward the test device, fed from the fixture on the bottom.

The fluidic data was obtained with an Agilent 34972A data acquisition system sampling every 10 s. Pressure taps, with pressure transducers (PX329-111A5V, Omega), in the fluid channels provided the upstream and downstream pressure of the microjets. Rugged pipe plug Type K thermocouples (TC-K-NPT-U-72, Omega) were inserted into 3/8-in Tee fittings (SS-600-3TTF, Swagelok) at the fluid inlet and outlet channels to measure fluid temperature. Micro-Raman thermography, discussed in the next section, was used to obtain surface temperature measurements of the test device. Shown in Fig. 4b is an exploded view of the fixture assembly that was used to evaluate the microjet-cooled test device. The cover plate, in addition to providing a compressive force to seal the O-rings, contained a 12.5 mm × 7.5 mm optical viewing port for the temperature measurement.

Also shown in Fig. 4a, the fixture was mounted to a movable XY stage. The high speed, motorized XY stage (MLS203-1, Thorlabs) can be moved in 0.1 μm increments. Customized software was developed to take temperature measurements, while stepping this stage in a mapping sequence. DC probe micro-manipulators, connected to a precision source/measure unit (B2902A, Agilent), were adjusted to apply power to the device.

The chiller (LCR-8-G2, K-O Concepts) delivered water to the microjets with a 20 °C setpoint and ±0.1 °C process control. A paddle flow meter (FTB321, Omega) was used to determine the flow rate, with a needle valve to control the flow rate. A sintered metal filter eliminated particles larger than 2 μm from the flow loop to prevent clogging of the microjet orifices and to protect the system pump.

A pressure vs. flow rate evaluation was conducted to understand the driving pressures necessary to achieve certain microjet velocities of interest. These results are shown in Fig. 4c. The flow velocity at the orifice of the microjets was calculated according to

$$V = \frac{\dot{V}}{N_j \left(\frac{\pi D^2}{4} \right)} \quad (2)$$

where V is the velocity at the microjet, \dot{V} is the flow rate in the loop, N_j is the number of microjets, and D is the diameter of the microjets. In Fig. 4c, instead of the usual paddle wheel flow meter, a Coriolis flow meter (Micro Motion CMFS025M, Emerson) was used to increase the accuracy of the flow characterization measurements (0.1% accuracy for the Coriolis flow meter compared to 5% for the paddle flow meter).

The pressure drop was calculated by subtracting the fluid outlet pressure from the fluid inlet pressure, measured with the pressure transducers placed in the pressure taps of the fixture. The needle valve was adjusted to achieve fine flow rate control. Fig. 4c shows that the driving pressure for a 16.93 m/s jet velocity (an overall flow rate of 204 mL/min) is approximately 30.4 psi. At the lower end of the range, the pressure drop was 1.9 psi to achieve a jet velocity of 3.65 m/s and a flow rate of 44 mL/min. A second order polynomial fit of the pressure drop to flow rate is shown in Fig. 4c.

The pressure vs. flow rate evaluation showed that microjets, producing high heat transfer coefficients, can be formed with modest flow rates (~ 10 mL/min per microjet) and driving pressure requirements (~10s of psi). These enable microjets to be parallelized for larger arrays of devices without enormous flow rate requirements. Moreover, the inherent parallelization of the microjets keeps system pressures highly practicable. In most experiments presented here, flow rates of only 200 mL/min were used for the circular array of 19 microjets.

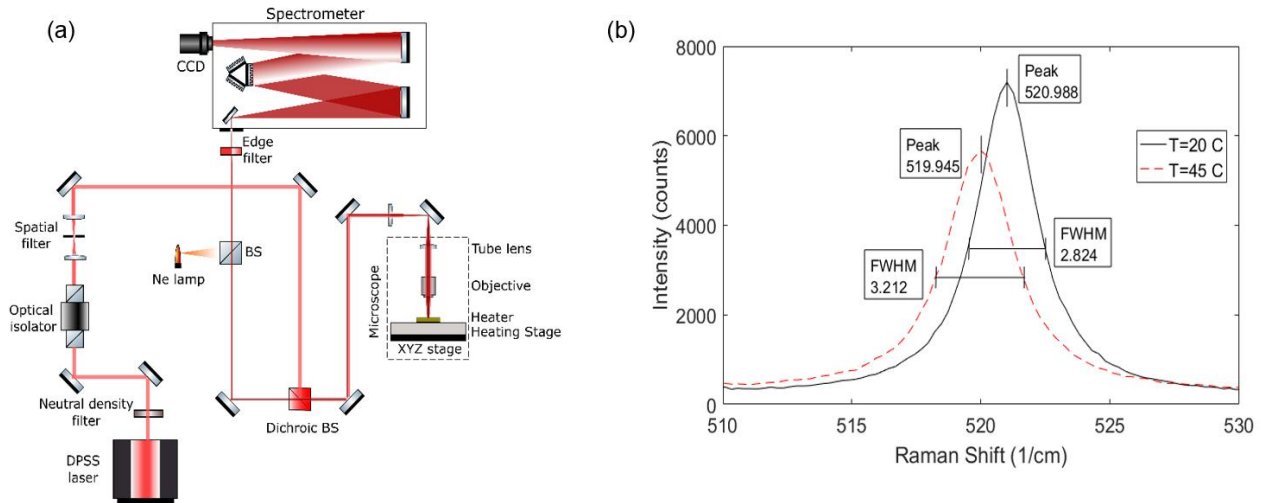


Fig. 5. (a) Schematic of free space optical setup, shown configured with a heating stage for calibration of Raman coefficients. The sample is illuminated by a laser coupled to a microscope, and the backscattered light is analyzed in the spectrometer. The sample is mounted to a movable XY stage, which allows for mapping of the surface temperature profile. (b) Raman spectra of silicon showing the peak (ω) and linewidth (Γ) decreasing and widening, respectively, with an increase in sample temperature from 20 °C to 45 °C.

B. Raman Thermography

To examine the performance of the embedded microjets, micro-Raman thermography was used to find the surface temperature profile of a fabricated test device. Micro-Raman thermography offers a promising technique to overcome the limited spatial resolution of IR cameras by using visible laser excitation with a diffraction limited spot size of $\sim 1 \mu\text{m}$ [25–26]. Variations of this technique have become increasingly popular for assessing temperature in silicon devices [27–28] and GaN HEMTs [29–30]. Here, micro-Raman thermography is used for the first time as an enabling tool for high spatial resolution characterization of a microfluidics system.

Micro-Raman thermography is derived from Raman spectroscopy and provides an accurate method for measuring device temperature with high spatial resolution. In the Raman scattering process, laser light focused at a spot on the sample with a wavelength λ_0 is scattered inelastically to a different wavelength λ due to optical phonon emission or absorption. The Raman scattered light analyzed by a spectrograph shows a peak with centroid $\omega = \lambda_0^{-1} - \lambda^{-1}$ labeled the Raman shift that is proportional to the phonon frequency for each optical phonon mode allowed by Raman scattering selection rules. The linewidth Γ of each peak is inversely proportional to the optical phonon lifetime of that particular mode [27]. The micro-Raman experimental setup used in this work is shown in Fig. 5a.

The micro-Raman measurements in this work were performed in the 180° backscattering configuration with a custom free space micro-Raman system consisting of a stabilized diode laser (SLM-FS, REO, $\lambda_0 = 632.9 \text{ nm}$), an optical microscope, and a 750 mm focal length spectrometer (Acton Spectra-Pro SP-2750, Princeton Instruments) along with an appropriate dichroic beam splitter and edge filter to separate the Raman scattered light from the laser excitation [29]. The $50\times$ microscope objective with a numerical aperture (NA) of 0.55 resulted in a lateral spot size of $\sim 1.4 \mu\text{m}$ and depth

of field (DoF) of $\sim 8.4 \mu\text{m}$. More details of micro-Raman spectroscopy and the measurement system are found in [29].

The Raman spectrum collected by the spectrometer and captured with the CCD (PIXIS 400BR, Princeton Instruments) shows a peak with a centroid at $\omega \cong 521 \text{ cm}^{-1}$ corresponding to the zone-center optical phonon frequency of the sample material, silicon. The linewidth or full width at half maximum (FWHM), Γ , of the peak is inversely proportional to the optical phonon lifetime. Because both the phonon frequency and lifetime are sensitive to temperature, temperature changes in the sample can be assessed by measured changes in the peak position and/or linewidth.

The Raman peak position shifted from 521 cm^{-1} to 520 cm^{-1} and the FWHM widened from 2.82 cm^{-1} to 3.21 cm^{-1} as the temperature increased from 20 °C to 45 °C. The peak position has been shown to have a linear dependence on temperature and stress as given by:

$$\omega - \omega_0 = A(T - T_0) + K(\sigma - \sigma_0) \quad (3)$$

where ω is the peak position at temperature T , ω_0 is the peak position at reference temperature T_0 , A is a material coefficient experimentally obtained through calibration, K is the stress coefficient, and σ and σ_0 are the stress states. It has been shown in the literature that the peak position's stress dependence includes both thermoelastic and inverse piezoelectric stress. To decouple the effects of temperature and stress on the Raman peak position, the Raman linewidth can also be used to deduce the temperature because the linewidth is much less sensitive to stress changes than peak position [27]. The linewidth has been observed to follow a quadratic dependence on the temperature according to:

$$\Gamma = B(T_T - T_0)^2 + C(T_T - T_0) + \Gamma_0 \quad (4)$$

where Γ is the linewidth at temperature T_T , Γ_0 is the linewidth at reference temperature T_0 , and B and C are material coefficients experimentally obtained with calibration.

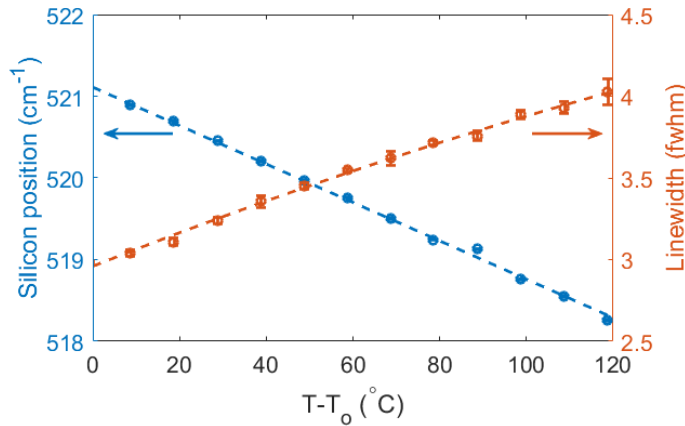


Fig. 6. Calibration of the Raman peak position and linewidth in the range of room temperature to 120 °C above room temperature

The Raman peak position coefficient, A , and the linewidth coefficients, B and C , were experimentally obtained with the optical setup shown in Fig. 5a. A temperature controlled stage (Mk1000, Instec) was used to bring the sample from room temperature (~ 20 °C) to 140 °C in increments of 10 °C. The measurements were completed with a 1 s exposure time with 3 averages and 5 repeats. The results of the calibration are shown in Fig. 6 with peak position in blue and linewidth in orange, as a function of temperature. The peak position was fitted with a first order polynomial and the linewidth was fitted with a second order polynomial.

Table I: Temperature Dependence of Raman Features

Coefficient	Value	Uncertainty	Units
A (3)	-0.0235	3.33×10^{-4}	cm^{-1}/K
B (4)	8.51×10^{-6}	1.95×10^{-5}	$\text{cm}^{-1}/\text{K}^2$
C (4)	9.18×10^{-3}	1.38×10^{-3}	cm^{-1}/K

Contained in Table I are the fitting parameters for both the Raman peak position and the linewidth as a function of temperature, in (3) and (4). The uncertainty of the parameter was calculated from the least squares fit.

The data collection process involved measuring the reference Raman peak position, ω_o , and linewidth, Γ_o , of the silicon heater in an unpowered state. The reference peak position was approximately 521 cm^{-1} and the reference linewidth was approximately 2.8 cm^{-1} . The precision source/measure unit applied a constant voltage across the probes and measured the resulting current. The temperature rise of the device was due to the Joule heat generation from the electric power applied to the heater; power from the laser (0.5 mW power at the device) has been shown to be a negligible source of measurement error in similar studies conducted at higher laser power levels [32–33]. The surface temperature was then calculated with both the Raman peak shift and linewidth broadening methods previously discussed, by solving (3) and (4) with the calibration coefficients A , B , and C . The uncertainty of the Raman temperature measurement was calculated according to the standard practice of vector summing outlined by Kline and McClintock [31]. At an elevated temperature of 45 °C, the

uncertainty of the temperature rise from the peak change was approximately ± 2 °C and the uncertainty of the temperature rise from the linewidth change was ± 5 °C.

V. RESULTS AND DISCUSSION

The microjets' heat transfer capability is based on how well they transfer heat energy per unit area and per unit temperature rise. This performance is quantified with the heat transfer coefficient, h , expressed as:

$$h = \frac{q}{S_j(T_s - T_f)} \quad (5)$$

where S_j is the jet impingement surface area, T_s is the temperature of the impingement surface (i.e., bottom of the silicon heater substrate), T_f is the local fluid temperature and q is the total energy dissipated within the device. As a derived quantity, heat transfer coefficients are difficult to measure directly. Instead, the heat transfer coefficients were extracted from the numerical model discussed in Section III. To substantiate the numerical results, detailed surface temperature measurements were taken with micro-Raman thermography. Strong agreement between surface temperature measurements and numerical results builds confidence in the predicted heat transfer coefficients. Additionally, peak temperatures can be obtained from both the numerical model and experimental measurements, providing direct information on a key driver of device reliability.

Heat transfer coefficients, extracted from the numerical model, are shown in Fig. 7 as color contours, while black circles indicate the location of the microjets as they exit their respective orifices. A steady heat rate of $q = 0.488 \text{ W}$ was applied to the top side of the heater's high resistance segments (1.95 W total, accounting for the quarter-symmetry model). The area shown is a $1 \text{ mm} \times 1 \text{ mm}$ square on the bottom face of the heater (i.e., the impingement surface).

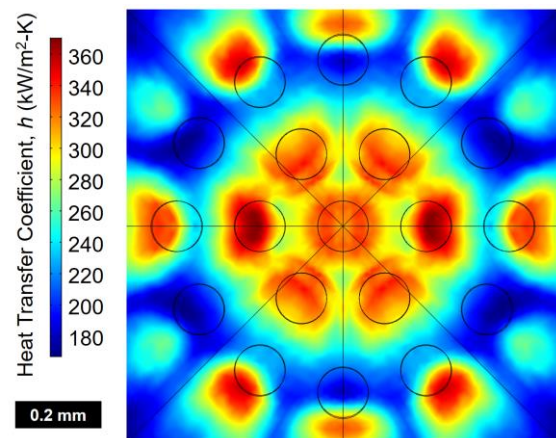


Fig. 7. Local convective heat transfer coefficient, h , in the $1 \text{ mm} \times 1 \text{ mm}$ region below the jet orifices. The average coefficient is $2.6 \times 10^5 \text{ W/m}^2\text{-K}$.

In Fig. 7, several observations were made. First, the microjets produced extremely high local heat transfer coefficients. The highest local heat transfer coefficients were approximately $380,000 \text{ W/m}^2\text{-K}$ located at the centerline of the central microjet

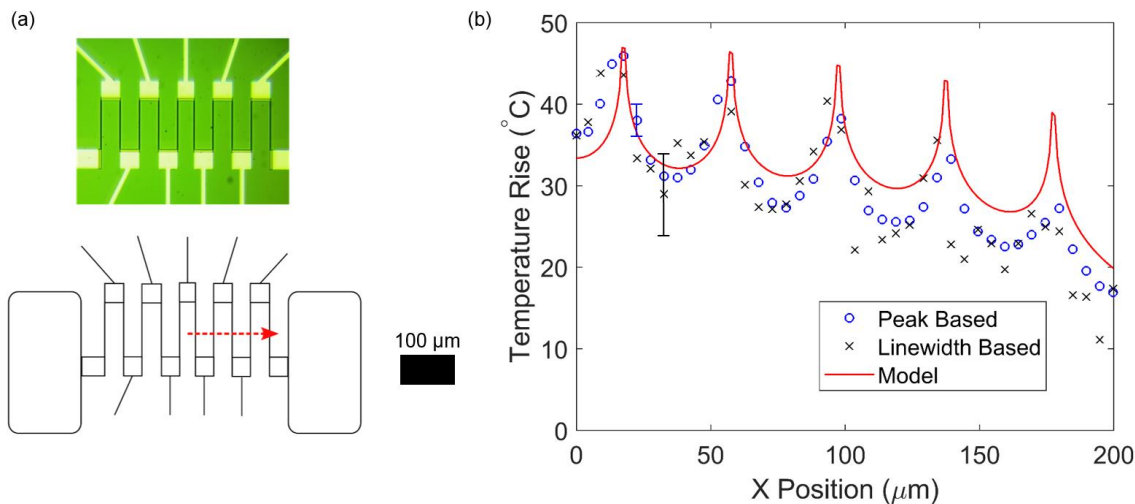


Fig. 8. (a) Top shows a microscope 10× image of the heater device showing the 10 finger-like segments. Bottom shows a schematic of the heater showing a horizontal slice (red dashed line) through the center. Also shown are the two contact pads used for applying power to the device. (b) Surface temperature of the device in a powered state (1.953 W) through the horizontal slice along the centerline, measured with both the Raman peak shift method (blue circles) and linewidth change method (black ×'s). Results from the coupled heat transfer and fluid dynamics model are shown with the solid red line.

cluster. The average heat transfer coefficient across the entire 1 mm × 1 mm square was 260,000 W/m²-K. Second, although excellent heat transfer was experienced with the central cluster of microjets, the outer ring of microjets exhibits some effects of washout—that is, the effluent from the central microjets deflected the outer microjets ever farther out in radius. More highly optimized array geometries could minimize this effect, and produce even higher average heat transfer coefficients.

To support these numerical results, micro-Raman thermography was used to obtain the corresponding surface temperature measurements. A known voltage difference was applied across the device, which resulted in Joule heating. The microjets impinged on the bottom surface of the test device, held in place with the fixture. Local temperature measurements were taken on the top (heat producing) surface of the test device. A schematic of the test device heater is in Fig. 8a. Being the center-most heater strip (or, “finger”), the sixth vertical strip in the sequence was expected to be the warmest. Fig. 8a also illustrates the detailed horizontal temperature slice through the center of the heater shown in Fig. 8b.

For the horizontal temperature slice shown in Fig. 8b, micro-Raman measurements were made at the vertical center of the device, located 50 μm through the 100 μm finger length. A surface temperature profile was taken using 5 μm increments from the middle of the device to the periphery. The temperature rise was calculated with the procedure of Section IV-B, using differences in both the Raman peak position (shown in blue circles) and linewidth (black ×'s). The Raman peak position shift method included the stress term in (3), whereas the linewidth method was stress independent but with higher uncertainty. Agreement between the two methods suggests that stress was not a contributing factor to the peak shift in this particular device, and thus both methods can be used to calculate the temperature of the device in the powered state.

Consistent with expectations, the measured temperatures exhibit a temperature rise when approaching the heater fingers (i.e., where the heat is being generated). Local minima are observed in between the heater fingers. Moreover, the global maximum, or peak, temperature is observed at the sixth (center-

most) heater finger, with decreasing finger temperatures away from the center of the heater. For a 1.95 W dissipation (a flux >5,000 W/cm²), the peak temperature rise was measured to be 45.9 ± 2 °C. Agreement with numerical predictions (solid red line in Fig. 8b) is good, lending strong support to the predicted heat transfer coefficients. Losses including heat conduction through the PEEK fixture and natural convection with free air at the heater surface, not accounted for in the model, may contribute to the model's overprediction of the heater's surface temperature, particularly at the periphery closest to the contact with the fixture. Additionally, somewhat lower measurements may be expected in the experiment due to the area enhancement of the jet plate pillars, which were not included in the numerical study. Future refinements to the computational model will include these contributors for comparison with the experiment.

VI. CONCLUSION

This work demonstrated the use of embedded microjets, integrated within an electronic device, for high performance thermal management. The approach implemented microjets in silicon, producing a thermal solution based on low-cost, industry-standard fabrication techniques and processes while remaining scalable for wafer-level production and integration.

Numerical modeling of the embedded microjets was used to predict thermal and fluidic performance. Because the microjets remain single phase throughout, the numerical study was computationally efficient and straightforward. The numerical results were corroborated with high fidelity micro-Raman thermography measurements, supporting the predicted heat transfer coefficients of 250,000 W/m²-K. Microjets can, therefore, produce a thermal solution with considerably higher thermal performance than traditional cold plate ($h \sim 10^3$ W/m²-K) or microchannel ($h \sim 10^4$ W/m²-K) implementations.

As demonstrated in this work, embedded microjet cooling is a highly effective, low SWaP-C thermal management solution for integrated, high power devices. Such an approach may be an enabling technology for a next generation of devices to reach higher powers, higher duty cycles, or higher frequency bands.

ACKNOWLEDGMENT

The authors would like to thank Mr. Timothy Hennighausen for his help in constructing the flow loop used in the experimental setup and bonding of the heater and jet plate dies. Additionally, the authors would like to thank Ms. Donna Yost and the MIT Lincoln Laboratory Microelectronics Laboratory for fabricating the heater devices and jet plates. The microjets program was supported by the MIT Lincoln Laboratory Radio Frequency Systems Line, led by Drs. Jeff Herd and Sean Duffy. The micro-Raman thermography system was supported by the Office of Naval Research (ONR) DURIP program under Dr. Mark Spector.

REFERENCES

- [1] A.L. Moore and L. Shi, "Emerging challenges and materials for thermal management of electronics", *Materials Today*, vol. 17, pp. 163–174, May 2014.
- [2] J. D. Blevins, G. D. Via, A. Bar-Cohen, and A. Sivananthan, "Developing a new thermal paradigm for gallium nitride (GaN) device technology", in *Proc. Compound Semicond. Mantech. Conf.*, Miami, FL, USA, May 2016, pp. 141–146.
- [3] V. Gambin, B. Poust, D. Ferizovic, M. Watanabe, and G. Mandrusiak, "Impingement cooled embedded diamond Multiphysics co-design," in *Proc.15th IEEE Intersoc. Conf. Thermal Thermomech. Phenomena Electron.Syst. (ITherm)*, Las Vegas, NV, USA, 2016, pp. 1518–1529.
- [4] D. Altman, A. Gupta, and M. Tyhach, "Development of a diamond microfluidics-based intra-chip cooling technology for GaN", in *Proc. ASME Internat. Tech. Conf. and Exhibition on Packaging and Integration of Electronic and Photonic Microsystems (InterPACK)*, San Francisco, CA, USA, 2015, pp. 1–7.
- [5] J. Ditri, J. Hahn, R. Cadotte, M. McNulty, and D. Luppa, "Embedded cooling of high heat flux electronics utilizing distributed microfluidic impingement jets," in *Proc. ASME Internat. Tech. Conf. and Exhibition on Packaging and Integration of Electronic and Photonic Microsystems (InterPACK)*, San Francisco, CA, USA, 2015, pp. 1–10.
- [6] J. Ditri, R. Cadotte, D. Fetterolf, and M. McNulty, "Impact of microfluidic cooling on high power amplifier RF performance," in *Proc.15th IEEE Intersoc. Conf. Thermal Thermomech. Phenomena Electron.Syst. (ITherm)*, Las Vegas, NV, USA, 2016, pp. 1501–1504.
- [7] H. Martin, "Heat and Mass Transfer Between Impinging Gas Jets and Solid Surfaces," *Adv. Heat Transfer*, vol. 13, pp. 1–60, 1977.
- [8] B. W. Webb and C.-F. Ma, "Single-Phase Liquid Jet Impingement Heat Transfer," *Adv. Heat Transfer*, vol. 26, pp. 105–217, 1995.
- [9] E. N. Wang, L. Zhang, L. Jiang, J.-M. Koo, J. G. Maveety, E. A. Sanchez, K.E. Goodson, and T.W. Kenny, "Micromachined Jets for Liquid Impingement Cooling of VLSI Chips," *J. Microelectromech. Syst.*, vol. 13, no. 5, pp. 833–842, Oct. 2004.
- [10] S. Ndao, Y. Peles, and M. K. Jensen, "Multi-Objective Thermal Design Optimization and Comparative Analysis of Electronics Cooling Technologies," *Int. J. Heat Mass Transfer*, vol. 52, pp. 4317–4326, Sep. 2009.
- [11] M. K. Sung and I. Mudawar, "Single-Phase and Two-Phase Hybrid Cooling Scheme for High-Heat-Flux Thermal Management of Defense Electronics," *ASME J. Electron. Packag.*, vol. 131, p. 021013, Jun. 2009.
- [12] G. J. Michna, E. A. Browne, Y. Peles, and M. K. Jensen, "Single-Phase Microscale Jet Stagnation Point Heat Transfer," *J. Heat Transfer*, vol. 131, p. 111402, Nov. 2009.
- [13] E. A. Browne, G. J. Michna, M. K. Jensen, and Y. Peles, "Experimental Investigation of Single-Phase Microjet Array Heat Transfer," *J. Heat Transfer*, vol. 132, p. 041013, Apr. 2010.
- [14] M. Fabbri and V. K. Dhir, "Optimized Heat Transfer for High Power Electronic Cooling Using Arrays of Microjets," *J. Heat Transfer*, vol. 127, no. 7, pp. 760–769, Nov. 2004.
- [15] T. Brunschwiler, H. Rothuizen, M. Fabbri, U. Kloter, B. Michel, R.J. Bezama, and G. Natarajan, "Direct liquid jet-impingement cooling with micron-sized nozzle array and distributed return architecture, in *Proc.10th IEEE Intersoc. Conf. Thermal Thermomech. Phenomena Electron.Syst. (ITherm)*, San Diego, CA, USA, 2006, pp. 196–203.
- [16] A.J. Robinson and E. Schnitzler. "An experimental investigation of free and submerged miniature liquid jet array impingement heat transfer," *Experimental Thermal and Fluid Sciences*, vol. 32, no. 1, pp. 1–13, Oct. 2007.
- [17] Y. Pan and B.W. Webb, "Heat transfer characteristics of arrays of free-surface liquid jets", *J. Heat Transfer*, vol. 117, no. 4, pp. 878–883, Nov 1995.
- [18] D.J. Womac, F.P. Incopera, and S. Ramadhyani, "Correlating equations for impingement cooling of small heat sources with multiple circular liquid jets", *J. Heat Transfer*, vol. 116, no. 2, pp. 482–486, May 1994.
- [19] D.J. Womac, S. Ramadhyani, and F.P. Incopera, "Correlating equations for impingement cooling of small heat sources with single circular liquid jets", *J. Heat Transfer*, vol. 115, no. 1, pp. 106–115, Feb. 1993.

[20] M. Garven and J. P. Calame, "Simulation and optimization of gate temperatures in GaN-on-SiC monolithic microwave integrated circuits," *IEEE Trans. Compon. Packag. Technol.*, vol. 32, no. 1, pp. 63–72, Mar. 2009.

[21] K. R. Bagnall, Y. S. Muzychka, E. N. Wang, "Analytical Solution for Temperature Rise in Complex Multilayer Structures With Discrete Heat Sources", *IEEE Trans. Components Packag. Manuf Technol.*, vol. 4, no. 5, pp. 817–830, 2014.

[22] D.C. Wilcox, "Formulation of the k- Ω turbulence model revisited", *AIAA Journal*, vol. 46, no. 11, pp. 2823–2838, Nov. 2008.

[23] W. Frie, "Which Turbulence Model Should I Choose for My CFD Application?", *COMSOL Blog*, Jul. 2017

[24] W. M. Kays, M. E. Crawford, and B. Weigand. *Convective Heat and Mass Transfer*, 4th ed. New York, NY, USA: McGraw-Hill, 2004.

[25] M. Kuball and J. W. Pomeroy, "A review of Raman thermography for electronic and optoelectronic device measurement with submicron spatial and nanosecond temporal resolution," *IEEE Trans. Device and Materials Reliability*, vol. 16, no. 4, pp. 667–684, Dec. 2016.

[26] A. Sarua, H. Ji, M. Kuball, M. J. Uren, T. Martin, K. P. Hilton, R. S. Balmer, "Integrated micro-Raman/infrared thermography probe for monitoring self-heating in AlGaIn/GaN transistor structures", *IEEE Trans. Electron Devices*, vol. 53, no. 10, pp. 2438–2447, Oct. 2006.

[27] T. Beechem, S. Graham, S. P. Kearney, et al., "Invited article: Simultaneous mapping of temperature and stress in microdevices using micro-Raman spectroscopy," *Review of Scientific Instruments*, vol. 78, p. 061301, Jun. 2007.

[28] S. P. Kearney, L. M. Phinney, and M. S. Baker, "Spatially resolved temperature mapping of electro-thermal actuators by surface Raman scattering," *J. Microelectromech. Syst.*, vol. 15, no. 2, pp. 314–321, Apr. 2006.

[29] K. R. Bagnall, E. A. Moore, S. C. Badescu, L. Zhang, and E. N. Wang, "Simultaneous measurement of temperature, stress, and electric field in GaN HEMTs with micro-Raman spectroscopy," *Review of Scientific Instruments*, vol. 88, p. 113111, Nov. 2017.

[30] T. Beechem, A. Christensen, S. Graham, and D. Green, "Micro-Raman thermometry in the presence of complex stresses in GaN devices," *J. Appl. Phys.*, vol. 103, p. 124501 Jun. 2008.

[31] S. Kline and F. McClintock, "Describing Uncertainties in Single-Sample Experiments," *Mechanical Engineering*, vol. 75, pp. 3–8, 1953.

[32] K. R. Bagnall, O. I. Saadat, S. Joglekar, T. Palacios, E. N. Wang, "Experimental Characterization of the Thermal Time Constants of GaN HEMTs Via Micro-Raman Thermometry", *IEEE Trans. Electron Devices*, vol. 64, no. 5, p. 2121, 2017.

[33] E. A. Moore, S. C. Badescu, L. Zhang, and E. N. Wang, "Simultaneous measurement of temperature, stress, and electric field in GaN HEMTs with micro-Raman spectroscopy," *Review of Scientific Instruments*, vol. 88, p. 113111, Nov. 2017.



Stephen M. Walsh (S'18) received the B.S. degree in mechanical engineering from the U.S. Naval Academy in Annapolis, MD, USA in 2016. He is currently pursuing the M.S. degree in mechanical engineering from the Massachusetts Institute of Technology (MIT), Cambridge, MA, USA.

Commissioned in May 2016, he is an ensign in the U.S. Navy. He is the recipient of a Lincoln Laboratory military fellowship where he works with the Structural and Thermal-Fluids Engineering Group. Additionally, he works in the Device Research Laboratory (DRL) at MIT. His research interests include high heat flux cooling, thermal metrology, and thermal issues in electronics.



Bernard A. Malouin Jr. received the B.S. degree in aeronautical and mechanical engineering as well as the Ph.D. degree in mechanical engineering from Rensselaer Polytechnic Institute, Troy, NY, USA, in 2006 and 2010, respectively.

Since 2011, he has been a member of the Technical Staff in the Structural and Thermal-Fluids Group at MIT Lincoln Laboratory in Lexington, MA, USA. Research interests include microfluidics for thermal applications, liquid optics, and interfacial fluid dynamics.

Dr. Malouin is also a member of the American Society of Mechanical Engineers (ASME) and the American Physical Society (APS).



Eric A. Browne received the B.S. degree in mechanical engineering as well as the Ph.D. degree in mechanical engineering from Rensselaer Polytechnic Institute, Troy, NY, USA, in 2006 and 2010, respectively.

Since 2014, he has been a member of the Technical Staff in the Structural and Thermal-Fluids Group at MIT Lincoln Laboratory in Lexington, MA, USA. Research interests include microfluidics for thermal applications, electronics cooling, and two phase heat transfer.



Kevin R. Bagnall received the B.S. degree in mechanical engineering from the University of Oklahoma, Norman, OK, USA, in 2009, and the M.S. and Ph.D. degrees in mechanical engineering from the Massachusetts Institute of Technology (MIT), Cambridge, MA, USA, in 2013 and 2017, respectively.

From 2011 to 2017, he was a Research Assistant with the Device Research Laboratory, Department of Mechanical Engineering, MIT. In 2014, he joined Analog Devices, Inc., Wilmington, MA, USA, as a Summer Intern. His current research interests include micro/nanoscale thermal transport, thermal issues in electronics, solid-state device physics, and thermal metrology techniques.

Dr. Bagnall was a recipient of the National Defense Science and Engineering Graduate Fellowship and the MIT Rohsenow Mechanical Engineering Graduate Fellowship.



Evelyn N. Wang received the B.S. degree in mechanical engineering from the Massachusetts Institute of Technology, Cambridge, MA, USA, in 2000, and the M.S. and Ph.D. degrees in mechanical engineering from Stanford University, Stanford, CA, USA, in 2001 and 2006, respectively.

From 2006 to 2007, she was a Post-Doctoral Researcher at Bell Laboratories, Alcatel-Lucent, Murray Hill, NJ, USA. She is currently the Gail E. Kendall Professor and the Associate Head with the Mechanical Engineering Department, Massachusetts Institute of Technology, Cambridge, MA, USA. Her current research interests include fundamental studies of micro and nano-scale heat and mass transport and the development of efficient thermal management, water desalination, and solar thermal energy systems.

Prof. Wang was a recipient of the 2012 ASME Bergles-Rohsenow Young Investigator Award in Heat Transfer and the 2017 ASME Gustus L. Larson Award.



James P. Smith received the B.S. degree in mechanical engineering and aeronautical engineering from Clarkson University, Potsdam, NY, USA in 2008. He received the M.S. and Ph.D. in mechanical engineering from Cornell University, Ithaca, NY, USA in 2013 and 2015, respectively.

From 2008 to 2009 he was a Mechanical Engineer at Lockheed Martin Space Systems. From 2009 to 2014 he was a Research Assistant in the Cornell Micro/Nanofluidics Laboratory. In 2015, he joined the Technical Staff of the Structural and Thermal-Fluids Group at MIT Lincoln Laboratory in Lexington, MA, USA. His research interests include microfluidics and the thermal management of high-power electronics.